Ultrasonic synthetic-aperture interface imaging

Van Der Neut, Joost; Fokkema, Jacob T.; Van Den Berg, Peter M.; Zapf, Michael; Ruiter, Nicole V.; Taskin, Ulas; Van Dongen, Koen W.A.

DOI
10.1109/TUFFC.2019.2903452

Publication date
2019

Document Version
Final published version

Published in
IEEE Transactions on Ultrasonics, Ferroelectrics, and Frequency Control

Citation (APA)
Van Der Neut, J., Fokkema, J. T., Van Den Berg, P. M., Zapf, M., Ruiter, N. V., Taskin, U., & Van Dongen, K. W. A. (2019). Ultrasonic synthetic-aperture interface imaging. *IEEE Transactions on Ultrasonics, Ferroelectrics, and Frequency Control*, *66*(5), 888-897. Article 8662631. https://doi.org/10.1109/TUFFC.2019.2903452

Ultrasonic Synthetic-Aperture Interface Imaging

Joost van der Neut, Jacob T. Fokkema, Peter M. van den Berg, Michael Zapf, Nicole V. Ruiter, Ulas Taskin, and Koen W. A. van Dongen

***Abstract*— Synthetic-aperture (SA) imaging is a popular method to visualize the reflectivity of an object from ultrasonic reflections. The method yields an image of the (volume) contrast in acoustic impedance with respect to the embedding. Typically, constant mass density is assumed in the underlying derivation. Due to the band-limited nature of the recorded data, the image is blurred in space, which is quantified by the associated point spread function. SA volume imaging is valid under the Born approximation, where it is assumed that the contrast is weak. When objects are large with respect to the wavelength, it is questionable whether SA volume imaging should be the method-of-choice. Herein, we propose an alternative solution that we refer to as SA interface imaging. This approach yields a vector image of the discontinuities of acoustic impedance at the tissue interfaces. Constant wave speed is assumed in the underlying derivation. The image is blurred in space by a tensor, which we refer to as the interface spread function. SA interface imaging is valid under the Kirchhoff approximation, where it is assumed that the wavelength is small compared to the spatial dimensions of the interfaces. We compare the performance of volume and interface imaging on synthetic data and on experimental data of a gelatin cylinder with a radius of 75 wavelengths, submerged in water. As expected, the interface image peaks at the gelatin–water interface, while the volume image exposes a peak and trough on opposing sides of the interface.**

***Index Terms*— Acoustic signal processing, image representation, ultrasonic imaging.**

I. Introduction

DUE to its computational simplicity, synthetic-aperture (SA) volume imaging is an attractive methodology to process ultrasonic reflection data [1], with a range of applications such as nondestructive testing [2] and breast imaging [3]. In SA volume imaging, the recorded signals are delayed in time and summed constructively over sources and receivers to generate an image of the internal reflectivity of an object. Hence, the method is also referred to as delay-and-sum beamforming.

SA volume imaging can be interpreted as a double (source and receiver) focusing process, which is closely related to filtered backpropagation [4] and (diffraction-stack) migration [5]. From a mathematical point of view, SA volume imaging is equivalent to the adjoint process of Born modeling [6]. Consequently, the constructed image can be interpreted as a contrast in acoustic impedance with respect to the embedding, which is blurred in space by an associated point spread function (PSF). Typically, a constant mass density is assumed, such that the contrast in acoustic impedance is effectively a contrast in wave speed. In Born inversion [7] or least-squares migration [8], we solve for the contrast by iterative inversion. SA imaging is merely the first iteration in this process.

When objects are large with respect to the wavelength, the scattered wavefield is dominated by specular reflections. In this regime, the complete volume contrast cannot be recovered and SA volume imaging yields an image of the object's boundary with suboptimal resolution. Various techniques have been proposed to improve the resolution under these conditions, such as (log-Gabor) filtering [9] or specular beamforming [10]. In this paper, we propose an alternative strategy by redefining the image in terms of an interface (rather than a volume) contrast. We start with a Kirchhoff-type forward model that we recently derived [11]. In this model, the object is characterized by a collection of interfaces, each having a unique orientation and reflection coefficient. By applying the adjoint of the modeling operator to the data, one can obtain an image of the interfaces. We show how this can be done effectively by modifying the familiar SA volume imaging algorithm. This results in SA interface imaging, having the potential to image large objects with superior resolution compared to SA volume imaging.

In Section II, we describe the underlying theory of SA volume imaging. In Section III, we introduce the modifications that are required to establish SA interface imaging. In Sections IV and V, we compare the performance of both methods on synthetic and experimental data, respectively. Special attention is paid to the finite frequency content of the data, which has important consequences for both methods. Although our methodology is not restricted to a particular geometry, we use circular arrays that are currently being developed for breast imaging [12]–[14] in all examples.

II. Volume Imaging

In Section II-A, we introduce a Born modeling operator to express the recorded data in terms of a volume contrast in acoustic impedance. In Section II-B, we evaluate the adjoint of this operator, which can be used for imaging. As shown in Section II-C, the constructed image is blurred in space by a PSF. Although all theories are derived for 3-D wave propagation, it can be easily modified for the 2-D case, as we discuss in Section II-D. Finally, we show in Section II-E how

Manuscript received December 6, 2018; accepted March 1, 2019. Date of publication March 7, 2019; date of current version April 24, 2019. This work was supported by ISES, The Netherlands Research Centre for Integrated Solid Earth Science. *(Corresponding author: Joost van der Neut.)*

J. van der Neut, J. T. Fokkema, P. M. van den Berg, U. Taskin, and K. W. A. van Dongen are with the Department of Imaging Physics, Faculty of Applied Sciences, Delft University of Technology, 2628 CJ Delft, The Netherlands (e-mail: j.r.vanderneut@tudelft.nl).

M. Zapf and N. V. Ruiter are with the Institute for Electronics and Data Processing, Karlsruhe Institute of Technology, 76021 Karlsruhe, Germany.

Digital Object Identifier 10.1109/TUFFC.2019.2903452

volume imaging can be realized efficiently in the time domain as a weighted sum over delayed signals.

A. Forward Model

Consider an unknown object within some finite spatial domain $\mathbb{D}$, enclosed by boundary $\partial\mathbb{D}$. The Cartesian position vector is defined as $\boldsymbol{x}=(x_1, x_2, x_3)$. Let c be the wave speed inside $\mathbb{D}$, while c_0 is the wave speed of the embedding. A constant mass density ρ_0 is assumed throughout space. A volume contrast is defined by $\chi = 1 - Z_0^2/Z^2$. Here, $Z=\rho_0\, c$ is the acoustic impedance, while $Z_0=\rho_0\, c_0$ is the acoustic impedance of the embedding. Our objective is to image the contrast from the scattered pressure field p^{sct}. We assume that the data obey a forward model, where $p^{\text{sct}} = p^{\text{sct}}(\boldsymbol{x}^R, \boldsymbol{x}^S, \omega)$ can be described by the volume integral [15]

$$p^{\text{sct}} = -\frac{\omega^2 Q(\omega)}{c_0^2} \int\limits_{\boldsymbol{x}\in\mathbb{D}} \mathrm{d}V\; G(\boldsymbol{x}-\boldsymbol{x}^R, \omega)\, G(\boldsymbol{x}-\boldsymbol{x}^S, \omega)\, \chi(\boldsymbol{x}) \quad (1)$$

where $\boldsymbol{x}^S$ and $\boldsymbol{x}^R$ denote the locations of the source and receiver, respectively. The source signature is given by Q and ω denotes the angular temporal frequency. Equation (1) is valid under the Born approximation, where it is assumed that the contrast is relatively weak, such that multiple scattering and phase shifts due to the contrast can be neglected [16]. All quantities can be transformed to the time domain with the inverse Fourier transform

$$\check{p}(t) = \frac{1}{\pi}\, \Re \int\limits_0^{+\infty} \mathrm{d}\omega\, \exp(j\omega t)\, p(\omega) \quad (2)$$

where $\check{}$ indicates the time domain, j is the imaginary unit, and t denotes time. In this definition, we have used positive frequencies only and $\Re$ should be interpreted as an operator that takes the real part of the quantity on its right-hand side. Symbol G represents Green's function for a homogeneous medium with wave speed c_0 and takes the familiar form [15]

$$G_{3D}(\boldsymbol{x}, \omega) = \frac{\exp(-j\omega|\boldsymbol{x}|/c_0)}{4\pi\,|\boldsymbol{x}|}. \quad (3)$$

In (3), and in some equations that follow, we have added a subscript 3-D to emphasize the validity for 3-D wave propagation only. In Section II-D, we show that the derived theory can also be applied to 2-D wave propagation problems, when all quantities with this subscript are replaced by their 2-D equivalents.

B. Backpropagation

In Born inversion or least-squares migration, (1) is typically solved by iterative inversion [8]. If we consider a single iteration only, the result is commonly referred to as backpropagation. Mathematically, this process is achieved by applying the adjoint of the modeling operator in (1) to the recorded data, which is equivalent to

$$-\frac{\omega^2\; Q^*(\omega)}{c_0^2} \oint\limits_{\boldsymbol{x}^R\in\partial\mathbf{D}} \mathrm{d}A\; G^*(\boldsymbol{x}-\boldsymbol{x}^R, \omega) \times \oint\limits_{\boldsymbol{x}^S\in\partial\mathbf{D}} \mathrm{d}A\; G^*(\boldsymbol{x}-\boldsymbol{x}^S, \omega)\; p^{\text{sct}}(\boldsymbol{x}^R, \boldsymbol{x}^S, \omega)$$

where superscript $*$ denotes the complex conjugation. In practice, the acquisition boundaries of sources and receivers are often incomplete. To account for such incompleteness in our formulation, we insert a function $\Delta(\boldsymbol{x}^R, \boldsymbol{x}^S)$ in the inner integrand. By definition, $\Delta = 1$ for those source–receiver combinations that are used (for recording), while $\Delta = 0$ for those combinations that are absent. Furthermore, we replace the factor ω^2/c_0^2 by a frequency-dependent weighting function H^{vol} that can be used to tune the methodology for a specific purpose. For instance, H^{vol} might include a deconvolution filter $1/(|Q|^2+\epsilon)$ (where ϵ is a small constant added for numerical stability) to optimize for resolution. An image is typically obtained by transforming the backpropagated field to the time domain and evaluating the result at zero time [17]. The result can also be interpreted as a weighted sum over frequencies. When we apply this procedure, we arrive at the following definition for the image $m^{\text{vol}} = m^{\text{vol}}(\boldsymbol{x})$:

$$m^{\text{vol}} = -\frac{1}{\pi}\, \Re \int\limits_0^{+\infty} \mathrm{d}\omega\; Q^*(\omega)\, H^{\text{vol}}(\omega) \oint\limits_{\boldsymbol{x}^R\in\partial\mathbf{D}} \mathrm{d}A\; G^*(\boldsymbol{x}-\boldsymbol{x}^R, \omega) \times \oint\limits_{\boldsymbol{x}^S\in\partial\mathbf{D}} \mathrm{d}A\; G^*(\boldsymbol{x}-\boldsymbol{x}^S, \omega)\; \Delta(\boldsymbol{x}^R, \boldsymbol{x}^S)\; p^{\text{sct}}(\boldsymbol{x}^R, \boldsymbol{x}^S, \omega) \quad (4)$$

where we used the inverse Fourier transform from (2), evaluated at $t=0$.

C. Point Spread Function

To interpret the image that is obtained by backpropagation, it appears convenient to substitute the forward model (1) into (4). The result can be written as

$$m^{\text{vol}} = \int\limits_{\boldsymbol{x}'\in\mathbb{D}} \mathrm{d}V\; B^{\text{vol}}(\boldsymbol{x}, \boldsymbol{x}')\, \chi(\boldsymbol{x}') \quad (5)$$

with

$$B^{\text{vol}} = \frac{1}{\pi}\, \Re \int\limits_0^{+\infty} \mathrm{d}\omega\; \frac{\omega^2 |Q(\omega)|^2 H^{\text{vol}}(\omega)}{c_0^2} \times \int\limits_{\boldsymbol{x}^R\in\partial\mathbf{D}} \mathrm{d}A\; G^*(\boldsymbol{x}-\boldsymbol{x}^R, \omega)\, G(\boldsymbol{x}'-\boldsymbol{x}^R, \omega) \times \int\limits_{\boldsymbol{x}^S\in\partial\mathbf{D}} \mathrm{d}A\; G^*(\boldsymbol{x}-\boldsymbol{x}^S, \omega)\, G(\boldsymbol{x}'-\boldsymbol{x}^S, \omega)\; \Delta(\boldsymbol{x}^R, \boldsymbol{x}^S). \quad (6)$$

From (5), we can learn that the image m^{vol} is blurred in space by the filter B^{vol}. More precisely, this filter quantifies the spatial smearing of a single (isolated) point scatterer in $\mathbb{D}$.

Hence, this filter is also known as the PSF [18]. When illumination is incomplete, the PSF can be used to quantify the angle-dependent illumination of an image point [19]. The PSF can also be used to assess the associated image m^{vol} of a given object χ [20] or to improve the resolution of an image by spatial deconvolution [21].

When illumination is complete [i.e., $\Delta(\boldsymbol{x}^R, \boldsymbol{x}^S) = 1$ for all $\boldsymbol{x}^R$ and $\boldsymbol{x}^S$], the PSF can be written in the following form:

$$B^{\text{vol}} = \frac{1}{\pi} \Re \int_0^{+\infty} \mathrm{d}\omega \, |Q(\omega)|^2 \, F^{\text{vol}}(\omega) \, H^{\text{vol}}(\omega) \times \Gamma^{\text{vol},R}(\boldsymbol{x}, \boldsymbol{x}', \omega) \, \Gamma^{\text{vol},S}(\boldsymbol{x}, \boldsymbol{x}', \omega) \quad (7)$$

where F^{vol} is a filter that depends solely on the temporal frequency

$$F_{3D}^{\text{vol}} = \frac{\omega^2}{16\pi^2 c_0^2} \quad (8)$$

while $\Gamma^{\text{vol},S}$ and $\Gamma^{\text{vol},R}$ are spatial blurring filters at the source and receiver sides, respectively. They are given by

$$\Gamma_{3D}^{\text{vol},S} = 4\pi \oint_{\boldsymbol{x}^S \in \partial\mathbf{D}} \mathrm{d}A \, G_{3D}^*(\boldsymbol{x} - \boldsymbol{x}^S, \omega) \, G_{3D}(\boldsymbol{x}' - \boldsymbol{x}^S, \omega) \quad (9)$$

and

$$\Gamma_{3D}^{\text{vol},R} = 4\pi \oint_{\boldsymbol{x}^R \in \partial\mathbf{D}} \mathrm{d}A \, G_{3D}^*(\boldsymbol{x} - \boldsymbol{x}^R, \omega) \, G_{3D}(\boldsymbol{x}' - \boldsymbol{x}^R, \omega). \quad (10)$$

It is well known in both ultrasound [22] and seismic [23] imagings that the spatial filters can be approximated by sinc functions

$$\Gamma_{3D}^{\text{vol},R} = \Gamma_{3D}^{\text{vol},S} \approx \operatorname{sinc}(\omega|\boldsymbol{x} - \boldsymbol{x}'|/c_0). \quad (11)$$

This result can be easily derived from the identity [24]

$$\oint_{\boldsymbol{x}'' \in \partial\mathbf{D}} \mathrm{d}A \, G^* \, (\boldsymbol{x} - \boldsymbol{x}'', \omega) \, G(\boldsymbol{x}' - \boldsymbol{x}'', \omega) \approx \tfrac{-c_0}{\omega} \Im \, G(\boldsymbol{x} - \boldsymbol{x}', \omega) \quad (12)$$

where $\Im$ denotes an operator that takes the imaginary part of the quantity on its right-hand side. Equation (11) can be verified by substituting (3) and (12) into (9) and (10), and using Euler's formula. The right-hand side of (12) is also referred to as the homogeneous Green's function [25], while the left-hand side has been studied exhaustively to analyze the process of constructive and destructive interference that underpins image reconstruction [26]. It should be noticed that $\Delta(\boldsymbol{x}^R, \boldsymbol{x}^S) = 1$ is not the only condition that can realize the required focusing of the PSF. For instance, in pulse-echo imaging [27] or poststack migration [28], this process is achieved with merely coinciding sources and receivers, i.e., $\Delta(\boldsymbol{x}^R, \boldsymbol{x}^S) = \delta(\boldsymbol{x}^R - \boldsymbol{x}^S)$, where δ is the Dirac delta function.

D. 2-D Implementation

In case of 2-D wave propagation, the equations that were derived in Sections II-A–II-C should be modified. First, the volume and surface integrals are to be replaced by surface and line integrals, respectively. Green's function takes the form [15]

$$G_{2D}(\boldsymbol{x}, \omega) = \frac{K_0(j\omega|\boldsymbol{x}|/c_0)}{2\pi} \quad (13)$$

where K_0 denotes the modified Bessel function of the zeroth kind. The temporal filter F^{vol} is frequency-independent $F_{2D}^{\text{vol}} = 1/16$, while the spatial blurring filters are

$$\Gamma_{2D}^{\text{vol},S} = \frac{-4\omega}{c_0} \oint_{\boldsymbol{x}^S \in \partial\mathbf{D}} \mathrm{d}l \, G_{2D}^*(\boldsymbol{x} - \boldsymbol{x}^S, \omega) \, G_{2D}(\boldsymbol{x}' - \boldsymbol{x}^S, \omega) \quad (14)$$

and

$$\Gamma_{2D}^{\text{vol},R} = \frac{-4\omega}{c_0} \oint_{\boldsymbol{x}^R \in \partial\mathbf{D}} \mathrm{d}l \, G_{2D}^*(\boldsymbol{x} - \boldsymbol{x}^R, \omega) \, G_{2D}(\boldsymbol{x}' - \boldsymbol{x}^R, \omega). \quad (15)$$

When we substitute (13) into (14) and (15), we find with the help of identity (12) that the spatial filters can be approximated by

$$\Gamma_{2D}^{\text{vol},R} = \Gamma_{2D}^{\text{vol},S} \approx J_0(\omega|\boldsymbol{x} - \boldsymbol{x}'|/c_0) \quad (16)$$

where J_0 is a Bessel function of the zeroth kind. This result is well known in the literature [29].

E. Implementation by Delay and Sum

SA volume imaging is typically realized by shifting the recorded data in time and summing over sources and receivers [1]. Since the shifting operation can be computed relatively fast, this is often a preferable strategy for large-scale problems. To derive such a time-domain algorithm from the theory of the previous sections, we substitute (3) into (4). The result can be written as

$$m^{\text{vol}} = \sum_{\boldsymbol{x}^S, \boldsymbol{x}^R} \frac{\check{\psi}^{\text{vol}}\left(\boldsymbol{x}^R, \boldsymbol{x}^S, \dfrac{|\boldsymbol{x} - \boldsymbol{x}^R| + |\boldsymbol{x} - \boldsymbol{x}^S|}{c_0}\right)}{16\pi^2 |\boldsymbol{x} - \boldsymbol{x}^R| |\boldsymbol{x} - \boldsymbol{x}^S|} \quad (17)$$

where we have replaced the integral by a sum over the available sources and receivers. In this formulation, $\check{\psi}^{\text{vol}} = \check{\psi}^{\text{vol}}(\boldsymbol{x}^R, \boldsymbol{x}^S, t)$ represents the available data in the time domain (which should be densely sampled or interpolated to achieve an accurate result), after cross correlation with the source signature Q and convolution with the weighting factor H^{vol}, that is,

$$\check{\psi}^{\text{vol}} = \frac{1}{\pi} \Re \int_0^{+\infty} \mathrm{d}\omega \, \exp(j\omega t) H^{\text{vol}}(\omega) Q^*(\omega) p^{\text{sct}}(\boldsymbol{x}^R, \boldsymbol{x}^S, \omega). \quad (18)$$

In practice, the factor $16\pi^2 |\boldsymbol{x} - \boldsymbol{x}^R| |\boldsymbol{x} - \boldsymbol{x}^S|$ in the denominator of (17) is often ignored [1].

III. Interface Imaging

In the following, we derive a theory for SA interface imaging. We start with the introduction of a Kirchhoff-type modeling operator in Section III-A. Imaging is then realized by applying the adjoint of this operator to the data, as discussed in Section III-B. The constructed image is blurred in space by a tensor, which we define as the interface spread function (ISF) in Section III-C. In Section III-D, we show how the theory (which is derived in 3-D) can be adapted for 2-D wave propagation problems. Finally, we discuss in Section III-E how interface imaging can be implemented effectively in the time domain by a weighted delay-and-sum approach.

A. Forward Model

Recently, we presented a forward model for interface modeling and inversion [11]. In this model, the medium is represented by a collection of piecewise-homogeneous subdomains. The acoustic impedance is constant in each subdomain, while the wave speed is constant throughout space. Under these conditions, the following integral representation can be derived for the scattered data $p^{\text{sct}} = p^{\text{sct}}(\boldsymbol{x}^R, \boldsymbol{x}^S, \omega)$:

$$p^{\text{sct}} \approx -2Q(\omega) \int_{\boldsymbol{x}\in\mathcal{S}} \mathrm{d}A\, \partial_l G(\boldsymbol{x}-\boldsymbol{x}^R, \omega) G(\boldsymbol{x}-\boldsymbol{x}^S, \omega)\, \nu_l(\boldsymbol{x}) \mathcal{R}(\boldsymbol{x}) \tag{19}$$

where $\mathcal{S}$ is a collection of all interfaces between adjacent subdomains. Each interface has a normal ν_l and a reflection coefficient $\mathcal{R} = (Z^+ - Z^-)/(Z^+ + Z^-)$, where Z^+ and Z^- represent the acoustic impedance at both sides of the interface. Einstein's summation convention has been applied (meaning that we sum over repeated indices). Equation (19) is valid under the Kirchhoff approximation [28], where it is assumed that the wavelength is small compared to the spatial dimensions of the interfaces.

B. Backpropagation

Under the assumption that $\mathcal{S}$ can be represented by a discrete mesh of interfaces, (19) can be used for modeling and inversion [11]. Alternatively, we can develop a backpropagation method for interface imaging by applying the adjoint of the modeling operator to the data. Formally, this adjoint is given by

$$-2Q^*(\omega) \oint_{\boldsymbol{x}^R\in\partial\mathbf{D}} \mathrm{d}A\, \partial_k G^*(\boldsymbol{x}-\boldsymbol{x}^R, \omega) \times \oint_{\boldsymbol{x}^S\in\partial\mathbf{D}} \mathrm{d}A\, G^*(\boldsymbol{x}-\boldsymbol{x}^S, \omega)\, p^{\text{sct}}(\boldsymbol{x}^R, \boldsymbol{x}^S, \omega).$$

To make our framework more flexible, we include the function Δ to account for incomplete acquisition and we replace the factor 2 by a more general frequency-dependent weighting function H^{int}. Akin to volume imaging, we construct the image $m_k^{\text{int}} = m_k^{\text{int}}(\boldsymbol{x}^K)$ as a weighted sum over frequencies, that is,

$$m_k^{\text{int}} = -\frac{1}{\pi} \Re \int_0^{+\infty} \mathrm{d}\omega\, Q^*(\omega) H^{\text{int}}(\omega) \oint_{\boldsymbol{x}^R\in\partial\mathbf{D}} \mathrm{d}A\, \partial_k G^*(\boldsymbol{x}-\boldsymbol{x}^R, \omega) \times \oint_{\boldsymbol{x}^S\in\partial\mathbf{D}} \mathrm{d}A\, G^*(\boldsymbol{x}-\boldsymbol{x}^S, \omega) \Delta(\boldsymbol{x}^R, \boldsymbol{x}^S)\, p^{\text{sct}}(\boldsymbol{x}^R, \boldsymbol{x}^S, \omega). \tag{20}$$

When we compare this result with the backpropagation method for volume imaging [i.e., (4)], the main difference is that a spatial derivative ∂_k is applied to the receiver-side Green's function. A similar derivative can be found in various ray-based imaging algorithms that are designed to image the derivative of acoustic impedance from reflection data [30], [31]. In such algorithms, this derivative is either evaluated in a fixed (typically the vertical) direction or normal to the interface. In our formulation, we evaluate the derivative in each spatial direction k. Consequently, the image m_k^{int} is a vector that quantifies the discontinuities of acoustic impedance at the tissue interfaces.

C. Interface Spread Function

To interpret the constructed image, it is useful to substitute (19) into (20). The result can be written as

$$m_k^{\text{int}} = \int_{\boldsymbol{x}'\in\mathcal{S}} \mathrm{d}A\, B_{kl}^{\text{int}}(\boldsymbol{x}, \boldsymbol{x}')\, \nu_l(\boldsymbol{x}')\, \mathcal{R}(\boldsymbol{x}') \tag{21}$$

with

$$B_{kl}^{\text{int}} = \frac{1}{\pi} \Re \int_0^{+\infty} \mathrm{d}\omega\, 2|Q(\omega)|^2 H^{\text{int}}(\omega) \times \int_{\boldsymbol{x}^R\in\partial\mathbf{D}} \mathrm{d}A\, \partial_k G^*(\boldsymbol{x}-\boldsymbol{x}^R, \omega)\, \partial_l' G(\boldsymbol{x}'-\boldsymbol{x}^R, \omega) \times \int_{\boldsymbol{x}^S\in\partial\mathbf{D}} \mathrm{d}A\, G^*(\boldsymbol{x}-\boldsymbol{x}^S, \omega)\, G(\boldsymbol{x}'-\boldsymbol{x}^S, \omega)\, \Delta(\boldsymbol{x}^R, \boldsymbol{x}^S). \tag{22}$$

From (21), we can learn that the vector image m_k^{int} is blurred in space by the tensor B_{kl}^{int}. More precisely, this tensor quantifies the spatial smearing in the direction k of a single (isolated) interface contrast with normal ν_l. Hence, we refer to this tensor as the ISF.

When all sources and receivers are available (i.e., $\Delta(\boldsymbol{x}^R, \boldsymbol{x}^S) = 1$ for all $\boldsymbol{x}^S$ and $\boldsymbol{x}^R$), (22) can be written as

$$B_{kl}^{\text{int}} = \frac{1}{\pi} \Re \int_0^{+\infty} \mathrm{d}\omega\, |Q(\omega)|^2 F^{\text{int}}(\omega) H^{\text{int}}(\omega) \times \Gamma_{kl}^{\text{int},R}(\boldsymbol{x}, \boldsymbol{x}', \omega)\, \Gamma^{\text{vol},S}(\boldsymbol{x}, \boldsymbol{x}', \omega). \tag{23}$$

In this formulation, F^{int} is a filter that depends solely on the temporal frequency

$$F_{3D}^{\text{int}} = \frac{\omega^2}{24\pi^2 c_0^2} \tag{24}$$

while $\Gamma^{\mathrm{vol},S}$ and $\Gamma^{\mathrm{int},R}_{kl}$ are spatial filters at the source and receiver sides. The source-side filter $\Gamma^{\mathrm{vol},S}$ is similar as in volume imaging and is given by (9). The receiver-side filter can be written as

$$\Gamma^{\mathrm{int},R}_{kl,3D} = \frac{3c_0^2}{\omega^2}\partial_k\partial_l'\Gamma^{\mathrm{vol},R}_{3D}(\boldsymbol{x},\boldsymbol{x}',\omega). \tag{25}$$

Note that we have scaled the equations such that the peak amplitude of the receiver-side filter is $\Gamma^{\mathrm{int},R}_{ll,3D}(\boldsymbol{x},\boldsymbol{x},\omega)=1$.

D. 2-D Implementation

After a few modifications, the formulations that were derived in the previous sections can also be applied for 2-D wave propagation problems. Filter $F^{\mathrm{int}}_{2D}=1/16$ is frequency-independent. Furthermore, we have

$$\Gamma^{\mathrm{int},R}_{kl,2D} = \frac{2c_0^2}{\omega^2}\partial_k\partial_l'\Gamma^{\mathrm{vol},R}_{2D}(\boldsymbol{x},\boldsymbol{x}',\omega) \tag{26}$$

where $\Gamma^{\mathrm{int},R}_{ll,2D}(\boldsymbol{x},\boldsymbol{x},\omega)=1$ is again satisfied.

E. Implementation by Delay and Sum

SA interface imaging can be efficiently realized in the time domain by a weighted sum over delayed traces. To facilitate this approach, we approximate the gradient of Green's function in (3) as

$$\partial_k G_{3D}(\boldsymbol{x},\omega) \approx \frac{-j\omega}{c_0}\frac{x_k}{|\boldsymbol{x}|}\frac{\exp(-j\omega|\boldsymbol{x}|/c_0)}{4\pi|\boldsymbol{x}|}. \tag{27}$$

After substituting (3) and (27) into (20), we arrive at

$$m^{\mathrm{int}}_k = \sum_{\boldsymbol{x}^S,\boldsymbol{x}^R}\frac{x_k-x^R_k}{|\boldsymbol{x}-\boldsymbol{x}^R|}\frac{\check{\psi}^{\mathrm{int}}\left(\boldsymbol{x}^R,\boldsymbol{x}^S,\dfrac{|\boldsymbol{x}-\boldsymbol{x}^R|+|\boldsymbol{x}-\boldsymbol{x}^S|}{c_0}\right)}{16\pi^2|\boldsymbol{x}-\boldsymbol{x}^R||\boldsymbol{x}-\boldsymbol{x}^S|} \tag{28}$$

where we replaced the integral by a sum over the available sources and receivers. The prefiltered data $\check{\psi}^{\mathrm{int}} = \check{\psi}^{\mathrm{int}}(\boldsymbol{x}^R,\boldsymbol{x}^S,t)$ are given by

$$\check{\psi}^{\mathrm{int}} = \frac{1}{\pi}\Re\int_0^{+\infty}\mathrm{d}\omega\,\exp(j\omega t)H^{\mathrm{int}}(\omega)Q^*(\omega) \times\left(\frac{-j\omega}{c_0}\right)p^{\mathrm{sct}}(\boldsymbol{x}^R,\boldsymbol{x}^S,\omega). \tag{29}$$

When we compare (28) and (29) with (17) and (18), we find two required modifications to turn an algorithm for volume imaging into an algorithm for interface imaging. First, an additional factor $-j\omega/c_0$ should be included during the prefiltering stage to realize the required derivative. Second, the traces should be weighted by an obliquity factor $(x_k-x^R_k)/|\boldsymbol{x}-\boldsymbol{x}^R|$ prior to summation. There is some analogy with various ray-based Kirchhoff migration algorithms, where a time derivative $-j\omega/c_0$ and an obliquity factor can also be found in the formulation [28]. In those algorithms, the obliquity factor is typically applied normal to the interface (yielding a scalar image) rather than in each spatial direction k (yielding a vector image).

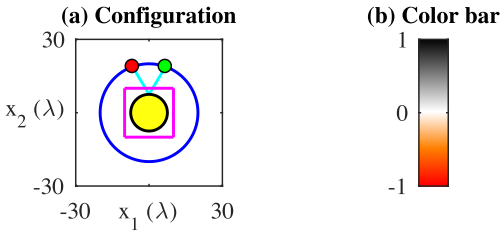

Fig. 1. (a) Configuration for the 2-D numerical study. The object is shown in yellow, while the blue circle denotes the array of sources and receivers. An arbitrary source and receiver pair is indicated by the red and green dot, respectively, where the cyan rays indicate the associated specular reflection path. The magenta box indicates the imaging domain. (b) Color bar that will be used throughout this paper.

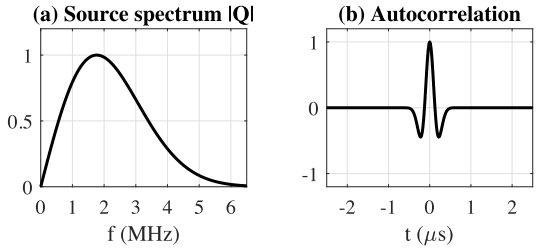

Fig. 2. (a) Spectrum of the source signature $|Q|$. (b) Autocorrelated source signature $|Q|^2$, transformed to the time domain.

IV. Numerical Study

In the following 2-D numerical simulation, we compare the performance of volume and interface imaging. In Section IV-A, we consider a source excitation with a relatively broad range of frequencies. In Section IV-B, we repeat the simulation with a band-limited source signal that is also used for the experimental study, as discussed later.

A. Broadband Excitation

The wave speed and the mass density of the embedding are $c_0=1500\,\mathrm{m/s}$ and $\rho_0=1000\,\mathrm{kg/m^3}$, respectively. As a source signal, we use the time derivative of a Gaussian, i.e., $Q(\omega)=j\omega\exp(-\omega^2/(2\pi f_m)^2)$, where $f_m=2.5$ MHz. We define the dominant wavelength as $\lambda=c_0/f_m=0.6\,\mathrm{mm}$. For convenience, we have computed all distances in units of λ. A cylindrical object with a radius of $7.5\,\lambda$ is located at the origin of a 2-D Cartesian coordinate system. The cylinder has a wave speed $c_1=1507.5\,\mathrm{m/s}$ and mass density $\rho_1=1005\,\mathrm{kg/m^3}$. This yields the following contrasts: $\chi_1=1-Z_0^2/Z_1^2\approx 0.02$ (with $Z_1=\rho_1\ c_1$) and $\mathcal{R}_1=(Z_1-Z_0)/(Z_1+Z_0)\approx 0.005$. A cylindrical array of 256 coinciding source and receiver locations encompasses the origin with a radius of $20\,\lambda$, see Fig. 1(a) for an illustration. For convenience, we show the color bar that will be used throughout this paper in Fig. 1(b). In Fig. 2(a), we show the frequency spectrum of the source signature Q. During the backpropagation, the source signature is autocorrelated by the action of Q^* in (4) and (20). In Fig. 2(b), we show the result of this operation (i.e., $|Q|^2$), transformed to the time domain. Ideally, we wish to see a narrow spike at $t=0$ with minimum sidelobes.

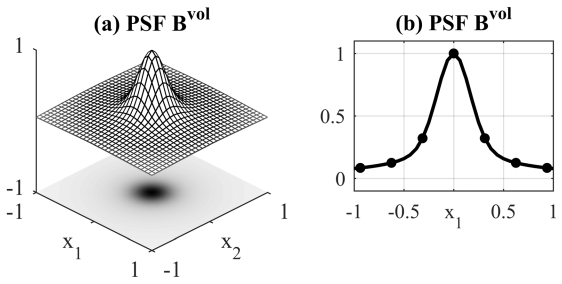

Fig. 3. (a) Numeric solution of the PSF as a function of x_1 and x_2. (b) Cross section of the PSF at $x_2 = 0$. The solid lines are the analytical solution, while the dots represent the numerical solution that was also shown in (a).

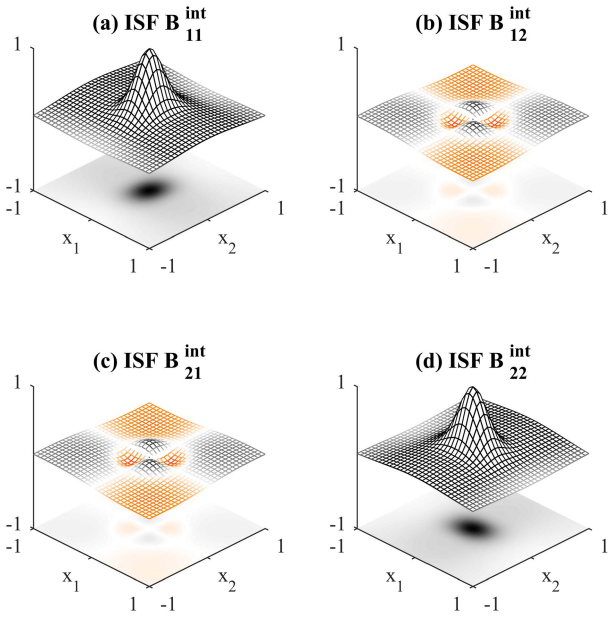

Fig. 4. Numerical solution of the ISF as a function of x_1 and x_2. (a) B_{11}^{int}. (b) B_{21}^{int}. (c) B_{21}^{int}. (d) B_{22}^{int}.

Based on the source signal and the source–receiver configuration, we computed the PSF by evaluating (6), where we made use of the 2-D Green's functions from (13). We used full coverage of sources and receivers and a constant weighting function $H_{2D}^{\text{vol}} = 16/A$, where $A = \pi^{-1}\,\Re\int_0^{+\infty} \mathrm{d}\,\omega |Q(\omega)|^2$. This particular choice for H^{vol} guarantees that the peak of the PSF equals unity. The result of the numerical simulation is shown in Fig. 3(a). We have also computed the PSF analytically by substituting (16) into (7). In Fig. 3(b), we compare the analytical and numerical solution, where we made a cross section at $x_2 = 0$. A good agreement is observed.

We proceed by computing the ISF with (22). Here, we have used a constant weighting function $H_{2D}^{\text{int}} = 16/A$ to ensure that the peak of the ISF equals unity. The result is shown in Fig. 4. Components B_{11}^{int} and B_{21}^{int}, which are shown in Fig. 4(a) and (b), describe the spatial blurring of an interface normal in the x_1-direction (which is placed at the origin) to interface normals in the x_1- and x_2-direction, respectively. Components B_{12}^{int} and B_{22}^{int}, which are shown in Fig. 4(c) and (d), describe the same phenomenon for an interface normal in the x_2-direction. We have also derived an analytical solution of the ISF. For this purpose, we evaluated the derivatives in (26) analytically and substituted the solution into (23). In Fig. 5, we compare the analytical and numerical solutions, where we made cross sections of B_{11}^{int} at $x_2 = 0$ and $x_1 = 0$. A good agreement is observed.

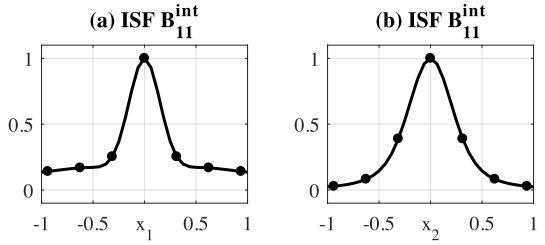

Fig. 5. Cross section of ISF component B_{11}^{int} at (a) $x_2 = 0$ and (b) $x_1 = 0$. The solid lines are the analytical solution, while the dots represent the numerical solution that was also shown in Fig. 4.

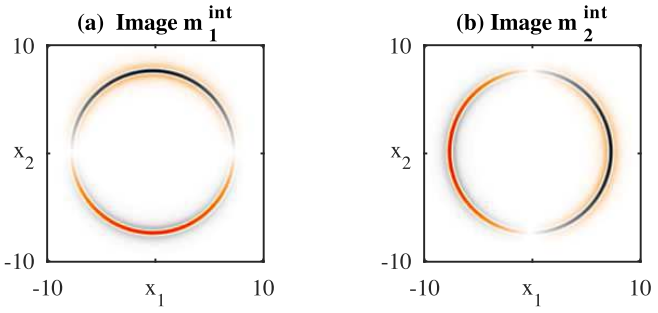

Fig. 6. Individual components of the interface image. (a) m_1^i. (b) m_2^i.

The scattered data p^{sct} have been computed analytically [15, Sec. 14.6]. A volume image is constructed with (4) and an interface image with (20). To ensure that we process only reflections (rather than transmissions), we set $\Delta = 0$ for all source–receiver combinations with an angle $\theta = \arccos\left(\boldsymbol{x}^R \cdot \boldsymbol{x}^S / (|\boldsymbol{x}^R||\boldsymbol{x}^S|)\right)$ exceeding 90°, following [29]. The two components of the interface image are shown in Fig. 6. To allow for a straightforward comparison with the volume image, we also computed the radial component of the interface image, which we define as $m^i = (x_k/|\boldsymbol{x}|)\, m_k^i$. The results of volume imaging and (radial) interface imaging are shown in Fig. 7. In Fig. 7(c) and (d), we zoomed-in view on a cross section that cuts through the interface, where normalization has been applied with respect to the peak amplitude of the signal's envelope. In the volume image, we observe positive and negative amplitudes of the signal on both sides of the interface (indicated in red), while the signal vanishes at the interface. In the interface image, we observe a clear peak at the interface. This peak is not perfectly symmetric. The asymmetry can be attributed to the wave speed contrast on both sides of the interface. This contrast is not properly handled as the underlying theory of interface imaging is based solely on a contrast in mass density [11]. Note that our result depends on the size of the object. To illustrate this, we repeat the experiment for a small cylinder in the Appendix.

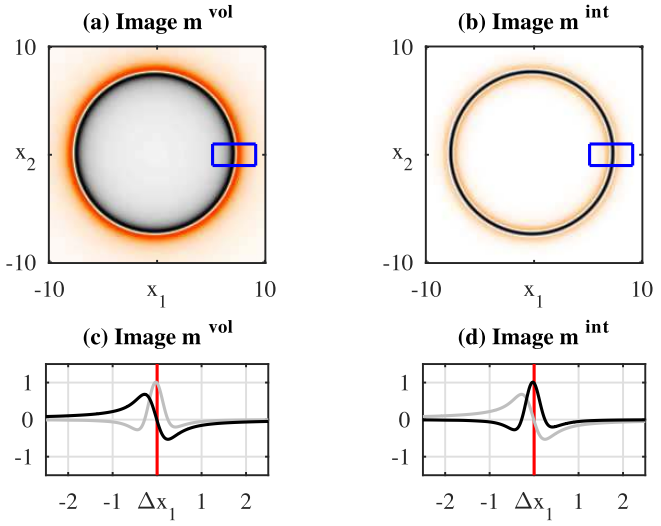

Fig. 7. (a) Volume and (b) (radial) interface image of the object. The areas in the blue boxes are enhanced in (c) and (d) (in black). These panels represent cross sections at $x_2 = 0$ and are centered around the interface location, i.e., $\Delta x_1 = x_1 - 7.5\lambda$. The red line indicates the location of the interface at $\Delta x_1 = 0$ (in gray, we show the interface image in the panel of the volume image and vice versa).

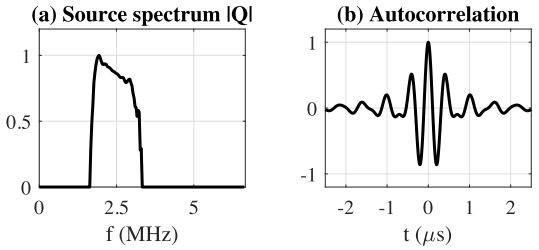

Fig. 8. Same as Fig. 2, when the excitation of the experimental study is used. (a) Source spectrum |Q|. (b) Autocorrelation.

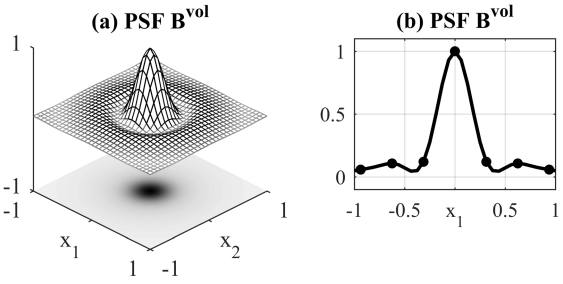

Fig. 9. Same as Fig. 3, when the excitation of the experimental study is used. (a) and (b) PSF B^{vol}.

B. Band-Limited Excitation

The frequency band of the experimental data that we will discuss later is significantly narrower than in the previous example. The excited spectrum is shown in Fig. 8(a). Akin to the spectrum that we considered so far, the excitation is centered around 2.5 MHz. However, no signal is emitted below 1.63 MHz and above 3.33 MHz. In Fig. 8(b), we show the autocorrelated source signature in the time domain. Note that the side lobes are significantly stronger than in the previous example. Figs. (9)–(11) show the PSF and ISF under similar conditions as in the previous section, given the source

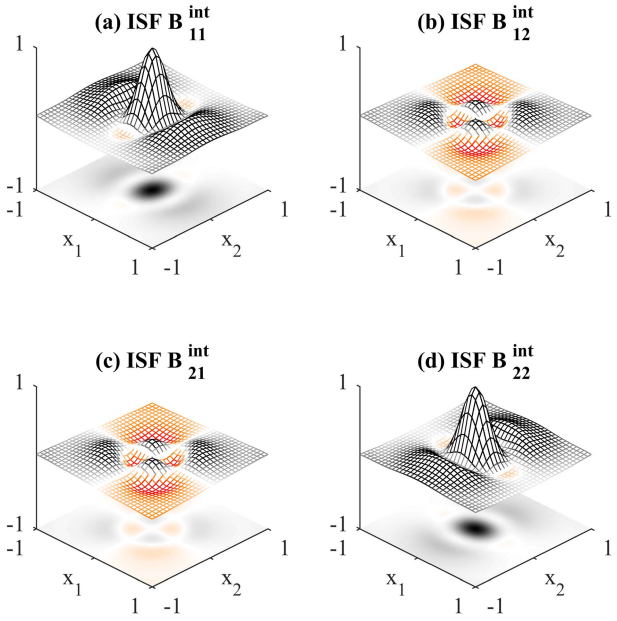

Fig. 10. Same as Fig. 4, when the excitation of the experimental study is used. (a) ISF B^{int}_{11}. (b) ISF B^{int}_{12}. (c) ISF B^{int}_{21}. (d) ISF B^{int}_{22}.

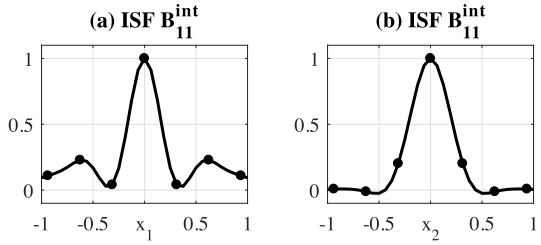

Fig. 11. Same as Fig. 5, when the excitation of the experimental study is used. (a) and (b) ISF B^{int}_{11}.

signature of the experimental study. Note that significant side lobes can be observed in both the PSF and ISF, due to the band-limited nature of the source excitation. Consequently, both the volume and interface image blur more significantly in space, as demonstrated in Figs. 12 and 13. Under these conditions, the improvement that interface imaging can bring over volume imaging is less apparent. What can be observed in Fig. 13(c) and (d), however, is that the peak of the interface image emerges at the interface, while the volume image vanishes at this location.

V. Experimental Study

In this section, we test our formulations for volume and interface imaging with experimental data from the ultrasound computer tomography (USCT) system that is developed at the Karlsruhe Institute of Technology [3]. As an object, we use a gelatin cylinder with a radius of approximately 75 λ. The cylinder is positioned roughly in the center of the spatial grid. Its actual horizontal location has been estimated as $(x_1, x_2) \approx (0.83\,\lambda, -1.70\,\lambda)$. We collected data from 1056 transducer array positions, which are indicated by the blue dots in Fig. 14(a). We selected 38 horizontal imaging

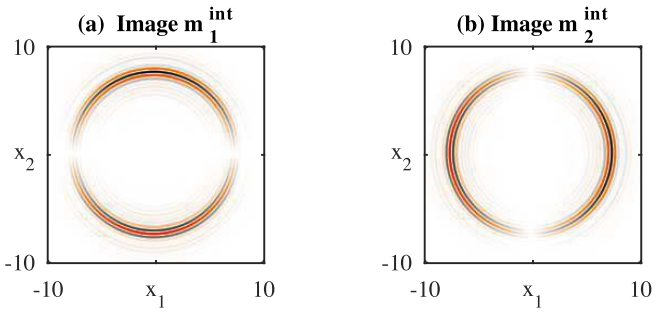

Fig. 12. Same as Fig. 6, when the excitation of the experimental study is used. (a) Image m_1^{int}. (b) Image m_2^{int}.

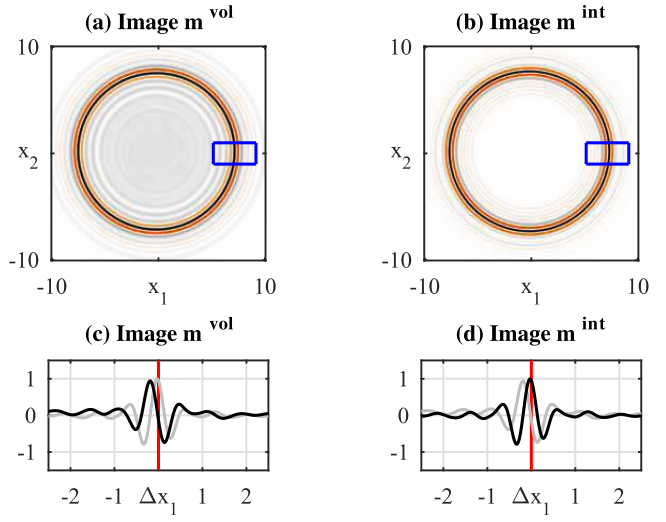

Fig. 13. Same as Fig. 7, when the excitation of the experimental study is used. (a) and (c) Image m^{vol}. (b) and (d) Image m^{int}.

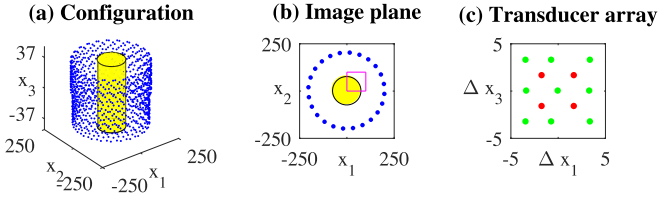

Fig. 14. (a) Configuration for the experimental study. The gelatin cylinder is shown in yellow. The 1056 transducer array positions are shown in blue. (b) One of the imaging planes (at $x_3 = 1\,\lambda$). The magenta box denotes the actual image that is shown in subsequent figures. The blue dots denote 24 transducer array positions that intersect the imaging plane. (c) Positioning of the sources (in red) and receivers (in green) at a single transducer array (Δx_1 and Δx_3 are relative distances with respect to the center of the array).

planes in the interval $x_3 \in [-37\,\lambda, 37\,\lambda]$. One of these planes is shown in Fig. 14(b). Each transducer array contains four sources and nine receivers. One of these arrays is shown in Fig. 14(c). For imaging, the same transducer array has been used in emit and receive. By this procedure, 38016 (1056×4×9) traces have been processed.

We have collected data with the source signature that we showed earlier in Fig. 8. The data have been upsampled to 40 MHz (in order to improve accuracy when imaging by delay and sum). Prior to imaging, we have applied residual time shifts to the recorded traces. For each source–receiver pair, we computed the travel time of the specular reflection and

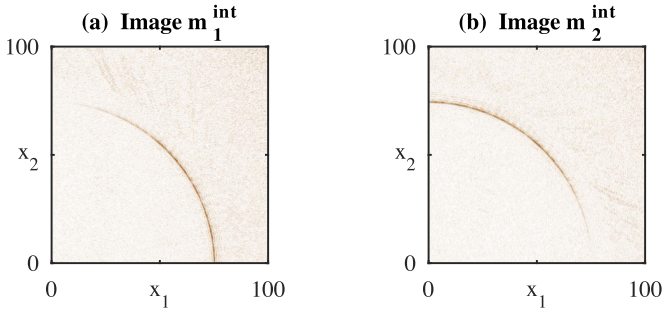

Fig. 15. Components of the interface image. (a) m_1^{int}. (b) m_2^{int}.

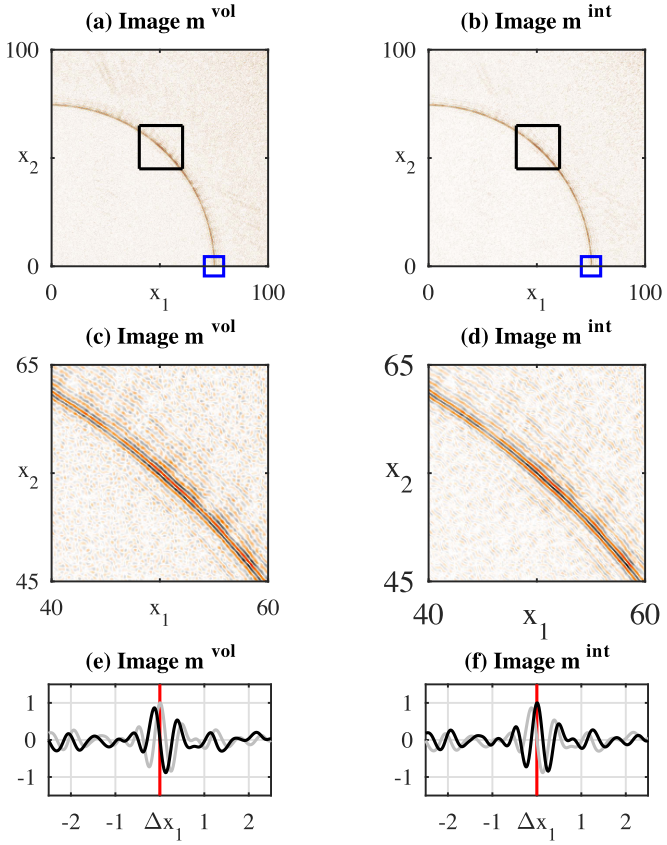

Fig. 16. (a) Volume and (b) interface image of the experimental data. (c) and (d) Zoomed-in view of the parts of the images that are indicated by the black boxes in (a) and (b). (e) and (f) Volume and interface images as a function of Δx_1 in a small window that is centralized at the interface (in black). This window is indicated by the blue boxes in (a) and (b). The red line indicates the location of the interface at $\Delta x_1 = 0$ (in gray, we show the interface image in the panel of the volume image and vice versa).

aligned the recorded signals accordingly. This allowed us to compensate for mismatch in wave speed, unknown electronic time delays, and deviations of the cylinder position. We used a constant wave speed $c_0 = 1501.5$ m/s. Averaging has been applied over the 38 imaging planes. In Fig. 15, we show the horizontal components of the interface image, which has been processed with the delay-and-sum method from Section III-E [we used (29) with $H^{\text{int}} = 1$ for prefiltering and (28) for imaging]. Note that only one quadrant of the cylinder has been imaged, as indicated in Fig. 14(b). We computed the radial component of the interface image (where we neglected the contribution of m_3^{int} and picked the origin at the center of the cylinder). In Fig. 16, we compare the result with an associated volume image, which is processed with the

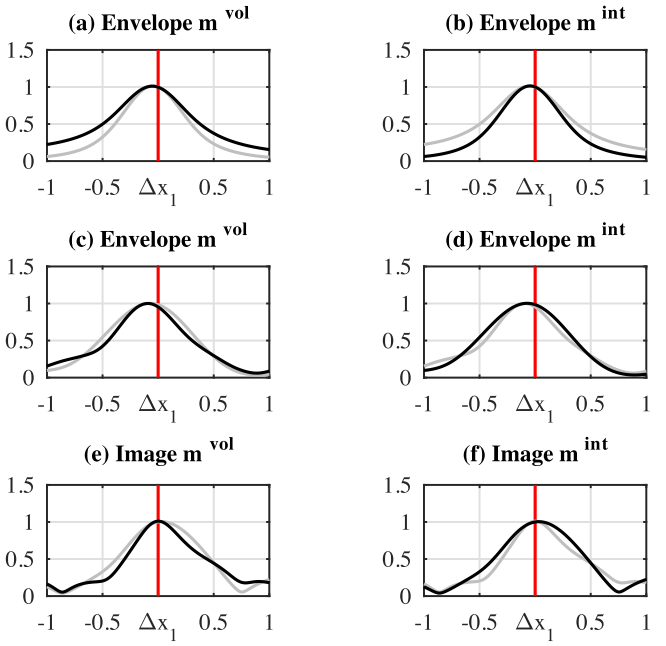

Fig. 17. Envelopes of the (a) volume and (b) interface image from the numerical study with broadband excitation (in black), (c) and (d) same with band-limited excitation, and (e) and (f) envelopes from the experimental study (in gray, we show the interface image in the panel of the volume image and vice versa).

delay-and-sum method from Section II-E [we used (18) with $H^{\text{vol}} = 1$ for prefiltering and (17) for imaging]. It is observed that the main lobe in the interface image coincides well with the actual location of the interface, while the volume image exposes a peak and trough on both sides of the interface. These observations confirm the conclusions that were drawn from the numerical study.

VI. Discussion

Volume and interface imaging are based on different assumptions and serve different purposes. We validated in Appendix that volume imaging yields a superior resolution when imaging a small object with a radius of $0.1\,\lambda$. For large objects, interface imaging has the potential to improve resolution if the band of emitted frequencies is sufficiently broad. To illustrate this, we plot the envelopes of the signals that were shown earlier [in Figs. 7(a) and (b), 13(a) and (b), and 16(e) and (f)] in Fig. 17. For broadband illumination, the envelope of the volume image [Fig. 17(a)] is wider than the envelope of the interface image [Fig. 17(b)]. This can be understood intuitively, as volume imaging is designed to reconstruct a volume contrast (which is nonzero throughout the cylinder), while interface imaging is designed to reconstruct the interface (which is nonzero only at the interface). However, the prospected effect seems insignificant when using the band-limited signal, as illustrated in Fig. 17(c) and (d). The same is observed in the experimental study, see Fig. 17(e) and (f). Hence, we can conclude that the success of interface imaging is currently obstructed by the narrow band of available frequencies. We remark that the studied contrast is relatively weak and that our conclusions may be different for a stronger contrast as, for instance, encountered in bone imaging.

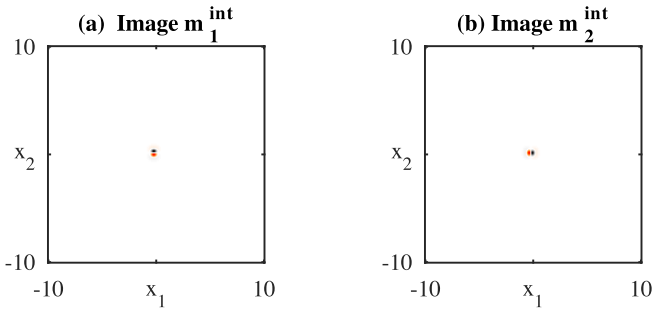

Fig. 18. Same as Fig. 6 for a cylinder with a radius of $0.1\,\lambda$. (a) Image m_1^{int}. (b) Image m_2^{int}.

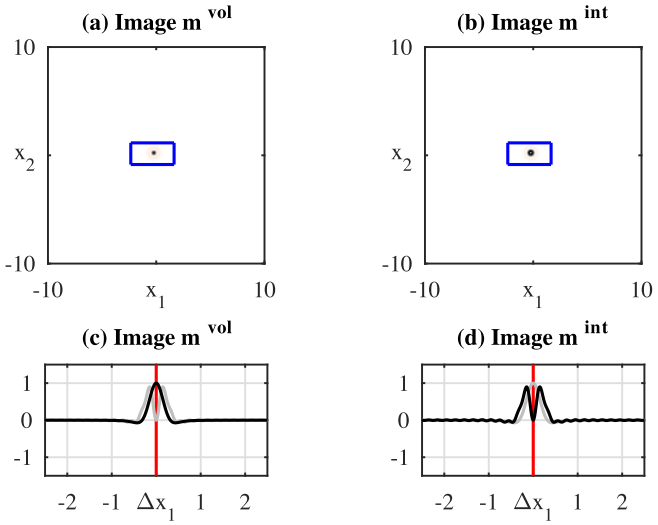

Fig. 19. Same as Fig. 7 for a cylinder with a radius of $0.1\,\lambda$. (a) and (c) Image m^{vol}. (b) and (d) Image m^{int}.

Since the interface image has a vector nature, it allows us to infer information not only on the magnitude of the acoustic impedance contrast but also on the orientations of potential interfaces. This information could aid the delineation of objects such as bones [32] or breast tumors [33]. The image can also be projected in an arbitrary direction in order to enhance or dim structures of a particular orientation.

Although our methodology has been derived in a background with constant wave speed, Green's functions that are used for backpropagation can also be computed (for instance, by finite-difference modeling) in a smooth background model, as is common practice in seismic imaging [34]. Alternatively, moderate wave speed variations can be accounted for by means of an aberration correction, which is sometimes applied in breast imaging [35]. Although we have focused our attention to circular arrays for breast imaging applications, the method can also be adapted to other configurations such as linear-array imaging. The effects of finite aperture that are posed by such configurations are considered beyond our scope but can easily be analyzed by computing the relevant PSF's and ISF's.

VII. Conclusion

We have presented a novel methodology for ultrasonic (SA) interface imaging and compared our approach with more conventional (SA) volume imaging. In volume imaging,

the contrast is a scalar that quantifies the acoustic impedance with respect to the embedding. In interface imaging, the contrast is a vector that quantifies the discontinuities of acoustic impedance at the tissue interfaces. With both methods, the constructed image can be interpreted as a blurred representation of the associated contrast. In volume imaging, blurring is described by a scalar, the PSF. In interface imaging, blurring is described by a tensor, the ISF. The interface image peaks accurately at the interface location, while the volume image displays a peak and trough on opposing sides of the interface. When a broad range of frequencies is emitted, interface imaging has the potential to delineate interfaces with superior resolution compared to volume imaging. When the bandwidth is limited and the contrast is weak as in our experimental study, the prospected resolution enhancement seems insignificant. This conclusion may depend on the strength and type (wave speed/mass density) of the contrast.

APPENDIX

If we repeat the numerical experiment in Section IV-A for a cylinder that is significantly smaller, the interfaces are to be imaged much closer to the origin. Consequently, the (positive and negative) interface contrasts start to interfere. We illustrate this effect for a cylinder of $0.1\,\lambda$ shown in Fig. 18. Under these conditions, the underlying assumptions of the Born approximation are met well. Consequently, volume imaging yields a single focal spot with a superior resolution [see Fig. 19]. In the interface image, we observe a band-limited ring (i.e., the interface) with an outer contour that is slightly broader than the focal spot in the volume image. Hence, volume imaging yields a superior resolution when imaging objects of this scale.

ACKNOWLEDGMENTS

The authors would like to thank T. Hopp, H. Gemmeke (Karlsruhe Institute of Technology, Karlsruhe, Germany), E. Janssen (Delft University of Technology, Delft, The Netherlands), and R. Govers (Erasmus University Medical Center) for stimulating discussions.

REFERENCES

[1] J. A. Jensen, S. I. Nikolov, K. L. Gammelmark, and M. H. Pedersen, "Synthetic aperture ultrasound imaging," *Ultrasonics*, vol. 44, pp. e5–e15, Dec. 2006.
[2] V. Schmitz, S. Chakhlov, and W. Muller, "Experiences with synthetic aperture focusing technique in the field," *Ultrasonics*, vol. 38, nos. 1–8, pp. 731–738, 2000.
[3] N. V. Ruiter, E. Kretzek, M. Zapf, T. Hopp, and H. Gemmeke, "Time of flight interpolated synthetic aperture focusing technique," *Proc. SPIE*, vol. 10139, p. 101390Q, Mar. 2017.
[4] A. J. Devaney, "A filtered backpropagation algorithm for diffraction tomography," *Ultrason. Imag.*, vol. 4, no. 4, pp. 336–350, 1982.
[5] G. Zhan, W. Dei, M. Zhou, Y. Luo, and G. T. Schuster, "Generalized diffraction-stack migration and filtering of coherent noise," *Geophys. Prospecting*, vol. 62, no. 3, pp. 427–442, 2014.
[6] D. Colton and R. Kress, *Inverse Acoustic and Electromagnetic Scattering Theory*. Berlin, Germany: Springer-Verlag, 1992.
[7] R. G. Keys and A. B. Weglein, "Genearalized linear inversion and the first Born theory for acoustic media," *J. Math. Phys.*, vol. 24, pp. 1444–1449, Jun. 1983.
[8] T. Nemeth, C. Wu, and G. T. Schuster, "Least-squares migration of incomplete reflection data," *Geophysics*, vol. 64, pp. 208–221, 1999.
[9] B. Zhuang, R. Rohling, and P. Abolmaesumi, "Directional log-gabor filtering on the pre-beamformed channel data to enhance hyper echoic structures," in *Proc. IEEE Int. Ultrason. Symp. (IUS)*, Sep. 2017, pp. 1–4.
[10] A. Rodriguez-Molares, A. Fatemi, L. Løvstakken, and H. Torp, "Specular beamforming," *IEEE Trans. Ultrason., Ferroelectr., Freq. Control*, vol. 64, no. 9, pp. 1285–1297, Sep. 2017.
[11] J. van der Neut, P. M. van den Berg, J. T. Fokkema, and K. W. A. van Dongen, "Acoustic interface contrast imaging," *Inverse Problems*, vol. 34, no. 11, pp. 115006-1–115006-15, 2018.
[12] N. Duric *et al.*, "Breast imaging with the SoftVue imaging system: First results," *Proc. SPIE*, vol. 8675, pp. 86750K-1–86750K-8, Mar. 2013.
[13] N. V. Ruiter, T. Hopp, M. Zapf, A. Menshikov, C. Kaiser, and H. Gemmeke, "3D ultrasound tomography for breast cancer diagnosis at KIT: An overview," in *Proc. Int. Workshop Med. Ultrasound Tomogr.*, Nov. 2017, pp. 205–216.
[14] J. Camacho *et al.*, "A multi-modal ultrasound breast imaging system," in *Proc. Int. Workshop Med. Ultrasound Tomogr.*, 2017, pp. 119–130.
[15] J. T. Fokkema and P. M. van den Berg, *Seismic Applications of Acoustic Reciprocity*. Amsterdam, The Netherlands: Elsevier, 1993.
[16] M. Born and E. Wolf, *Principles of Optics*. London, U.K.: Pergamon Press, 1965.
[17] J. F. Claerbout, *Fundamentals of Geophysical Data Processing*. New York, NY, USA: McGraw-Hill, 1976.
[18] L.-J. Gelius, I. Lecomte, and H. Tabti, "Analysis of the resolution function in seismic prestack depth imaging," *Geophys. Prospecting*, vol. 50, pp. 505–515, Sep. 2002.
[19] X.-B. Xie, S. Jin, and R.-S. Wu, "Wave-equation based seismic illumination analysis," *Geophysics*, vol. 71, pp. S169–S177, Aug. 2006.
[20] G. Toxopeus, J. Thorbecke, K. Wapenaar, S. Petersen, E. Slob, and J. Fokkema, "Simulating migrated and inverted seismic data by filtering a geological model," *Geophysics*, vol. 73, no. 2, pp. T1–T10, 2008.
[21] J. Yu, J. Hu, G. T. Schuster, and R. Estill, "Prestack migration deconvolution," *Geophysics*, vol. 71, pp. S53–S62, Mar. 2006.
[22] S. J. Norton and M. Linzer, "Ultrasonic reflectivity imaging in three dimensions: Reconstruction with spherical transducer arrays," *Ultrason. Imag.*, vol. 1, pp. 210–231, Jul. 1979.
[23] J. Chen and G. T. Schuster, "Resolution limits of migrated images," *Geophysics*, vol. 64, pp. 1046–1053, Jul. 1999.
[24] K. Wapenaar and J. Fokkema, "Green's function representations for seismic interferometry," *Geophysics*, vol. 71, pp. SI33–SI46, Jul./Aug. 2006.
[25] G. T. Schuster and J. Hu, "Green's function for migration: Continuous recording geometry," *Geophysics*, vol. 65, pp. 167–175, Jan./Feb. 2000.
[26] J. Thorbecke and K. Wapenaar, "On the relation between seismic interferometry and the migration resolution function," *Geophysics*, vol. 72, pp. T61–T66, Nov./Dec. 2007.
[27] S. J. Norton and M. Linzer, "Ultrasonic reflectivity imaging in three dimensions: Exact inverse scattering solutions for plane, cylindrical, and spherical apertures," *IEEE Trans. Biomed. Eng.*, vol. BME-28, no. 2, pp. 202–220, Feb. 1981.
[28] N. Bleistein, J. K. Cohen and J. W. Stockwell, *Mathematics of Multidimensional Seismic Imaging, Migration, and Inversion*. New York, NY, USA: Springer-Verlag, 2001.
[29] S. J. Norton and M. Linzer, "Ultrasonic reflectivity tomography: Reconstruction with circular transducer arrays" *Ultrason. Imag.*, vol. 1, pp. 154–184, Apr. 1979.
[30] N. Bleistein, "On the imaging of reflectors in the earth," *Geophysics*, vol. 52, pp. 931–942, Jul. 1987.
[31] P. Docherty, "A brief comparison of some Kirchhoff integral formulas for migration and inversion," *Geophysics*, vol. 56, pp. 1164–1169, Aug. 1991.
[32] I. Hacihaliloglu, R. Abugharbieh, A. J. Hodgson, and R. N. Rohling, "Bone surface localization in ultrasound using image phase-based features," *Ultrasound Med. Biol.*, vol. 35, pp. 1475–1487, Sep. 2009.
[33] W. Yang, S. Zhang, Y. Chen, W. Li, and Y. Chen, "Shape symmetry analysis of breast tumors on ultrasound images," *Comput. Biol. Med.*, vol. 39, pp. 231–238, Mar. 2009.
[34] G. A. McMechan, "Migration by extrapolation of time-dependent boundary values," *Geophys. Prospecting*, vol. 31, no. 3, pp. 413–420, 1983.
[35] N. V. Ruiter, R. Schnell, M. Zapf, and H. Gemmeke, "Phase aberration correction for 3D ultrasound computer tomography images," in *Proc. IEEE Ultrason. Symp. (IUS)*, Oct. 2007, pp. 1808–1811.

Authors' photographs and biographies not available at the time of publication.